

# Reversible proton co-intercalation boosting zinc-ion adsorption and migration abilities in bismuth selenide nanoplates for advanced aqueous batteries

Lei Peng<sup>a,b,c,1</sup>, Xiaochuan Ren<sup>a,b,1</sup>, Zhaofeng Liang<sup>a,b,1</sup>, Yuanhe Sun<sup>a,b,c,1</sup>, Yuanxin Zhao<sup>a,b</sup>, Jiaqian Zhang<sup>a,b</sup>, Zeying Yao<sup>a,b,c</sup>, Zhiguo Ren<sup>a,b</sup>, Zhao Li<sup>a,b</sup>, Juan Wang<sup>a,b</sup>, Beien Zhu<sup>a,b</sup>, Yi Gao<sup>a,b</sup>, Wen Wen<sup>a,b</sup>, Yaobo Huang<sup>a,b</sup>, Xiaolong Li<sup>a,b</sup>, Renzhong Tai<sup>a,b</sup>, Ke Yang<sup>a,b</sup>, Daming Zhu<sup>a,b,\*</sup>

<sup>a</sup> Shanghai Institute of Applied Physics, Chinese Academy of Sciences, Shanghai 201800, China

<sup>b</sup> Shanghai Synchrotron Radiation Facility, Shanghai Advanced Research Institute, Chinese Academy of Sciences, Shanghai 201204, China

<sup>c</sup> University of Chinese Academy of Sciences, Beijing 100049, China

## ARTICLE INFO

### Keywords:

(Aqueous zinc-ion battery  
Bismuth selenide nanoplates  
In situ synchrotron radiation-based X-ray diffraction  
Density functional calculations)

## ABSTRACT

Rechargeable aqueous zinc-ion batteries present low-cost, safe, and environmentally-friendly battery technology but suffer from the limited choice of cathode materials because of the sluggish kinetics of divalent zinc-ion associated with the high adsorption and migration energy barrier. Herein, a reversible zinc/bismuth selenide mild aqueous system was demonstrated for the first time, where bismuth selenide nanoplate cathode delivers a high specific capacity of 263.2 mA h g<sup>-1</sup> at 0.1 A g<sup>-1</sup> and robust rate capability of 100.6 mA h g<sup>-1</sup> even at 10 A g<sup>-1</sup> with long-term lifespan (82.3% retention after 1000 cycles). Benefiting from the layered structure and nanoplate morphology of the bismuth selenide cathode, surface-dominated ion storage is verified by a quantitative kinetics analysis, particularly at high current rates. Notably, unlike conventional batteries with only the reversible intercalation of alkali ions into metal chalcogenides, zinc/bismuth selenide aqueous batteries possess a sequential proton and zinc-ion insertion/extraction process, identified by *in situ* synchrotron radiation-based X-ray diffraction. Density functional theory analysis approves the low adsorption energy and preferential embedding process of protons, and that can further optimize Zn<sup>2+</sup> adsorption and migration abilities in bismuth selenide nanoplate, which is mainly responsible for the excellent performance.

## 1. Introduction

Lithium-ion batteries (LIBs) have been widely studied and applied in portable electronic devices and grid energy storage systems because of their high energy density.[1, 2] However, due to the shortage and high cost of lithium resources, the sustainability of LIBs is limited.[3–5] Moreover, the complex manufacturing and potential thermal runaway with the use of organic electrolytes in LIBs not only increases the battery cost but also causes safety hazards.[6] Rechargeable aqueous batteries are promising alternatives since aqueous electrolytes naturally contribute to increase in safety, cost-effectiveness and ionic conductivity compared to those of organic electrolytes.[7, 8] Zn-ion batteries (ZIBs) have been thoroughly studied from the ancient Volta battery to currently used rechargeable batteries due to their nontoxicity, stability, high theoretical capacity and the low redox potential of Zn/Zn<sup>2+</sup>

(-0.76 V vs. standard hydrogen electrode).[9, 10] Many studies have been performed to select suitable electrode materials to promote the practical application of aqueous ZIBs, such as manganese-based materials,[11] vanadium-based compounds and Prussian blue analogues.[12, 13] However, the low capacity, undesirable ionic conductivity, and poor cycling performance weaken the potential application of these cathode materials in ZIBs.[14–16] For example, the Jahn-Teller distortion in manganese-based cathodes and the rapid dissolution of active material in vanadium-based ZIBs lead to both having short lifespans. The Prussian blue analogue has a high discharge voltage (>1.7 V), but its discharge specific capacity is generally lower than 130 mA h g<sup>-1</sup>. [15] In light of these poor qualities, the development of new materials for ZIB cathodes is still in high demand.

Metal chalcogenides, due to their high electrical conductivity, thermal stability and natural abundance,[17] have been increasingly studied

\* Corresponding author at: Shanghai Synchrotron Radiation Facility, Shanghai Advanced Research Institute, Chinese Academy of Sciences, Shanghai 201204, China  
E-mail address: [zhudaming@zjlab.org.cn](mailto:zhudaming@zjlab.org.cn) (D. Zhu).

<sup>1</sup> These authors contributed equally to this work

for use in alkali-ion batteries; furthermore, metal chalcogenides may be utilized as promising cathodes in aqueous ZIBs due to being more electrochemically reversible and having faster charge transfer kinetics than their metal oxide counterparts.[18, 19] More recently, MoS<sub>2</sub> and VS<sub>2</sub>, the most common metal chalcogenides, have been proposed as host materials for reversible zinc-ion intercalation.[19, 20] Benefiting from the sufficient interplanar spacing of MoS<sub>2</sub> and VS<sub>2</sub>, a reversible Zn<sup>2+</sup> storage reaction and suitable redox potential, along with a capacity of approximately 200 mA h g<sup>-1</sup> and a cycling life of more than 200 cycles can be achieved; thus, these materials demonstrate the enormous potential of metal chalcogenides in aqueous ZIB cathodes. Nonetheless, the performance of reported metal chalcogenides is still unsatisfactory, especially their low capacity and poor rate capability, which deteriorates due to the high energy barrier of Zn<sup>2+</sup> intercalation (strong Coulombic ion-lattice interactions).[21–23] On the other hand, other than the conventional Zn<sup>2+</sup> shuttle mechanism, reversible proton co-intercalation has been detected in some cases of Mn or V-based oxide cathodes; this process is the main contribution to the high capacity and rate of the zinc aqueous system.[8, 24] To date, the dual-carrier intercalation process has seldom been demonstrated in metal chalcogenide cathodes, including cathodes of MoS<sub>2</sub> and VS<sub>2</sub>. The exhibited reversible co-intercalation of protons will not only boost the capacity but also may improve the zinc-ion storage performance by weakening the Coulombic ion-lattice interactions.[25] Therefore, feasible metal chalcogenide cathodes that are able to carry out proton and zinc-ion dual-carrier insertion/extraction processes at a high capacity and with well-established energy storage mechanisms should be highly considered and developed as cathode materials.

Bismuth selenide (Bi<sub>2</sub>Se<sub>3</sub>), a typical metal chalcogenide with a low band gap and a van der Waals crystal structure, exhibits remarkable thermoelectric and photoelectric properties and has been recognized as an efficient host material for lithium/sodium ions.[26–29] More importantly, the layered nanostructures of Bi<sub>2</sub>Se<sub>3</sub> increases stability while providing good carrier migration capability and proper layer spacing; thus, Bi<sub>2</sub>Se<sub>3</sub> may be an ideal cathode for ZIBs and a conceivable metal chalcogenide parasitifer for steady proton and zinc-ion insertion/extraction. However, until now, the zinc/bismuth selenide aqueous battery system has not been established and vacant for its energy storage mechanisms. Here, thin Bi<sub>2</sub>Se<sub>3</sub> nanoplates (TBSNs) with a uniform thickness (~5 nm) and good stability under circumstance condition are synthesized and introduced as aqueous ZIB cathodes for the first time. The as-prepared TBSNs exhibit a high discharge specific capacity of 263.2 mAh g<sup>-1</sup> at a current density of 0.1 A g<sup>-1</sup>. More importantly, adequate cycling stability with a high capacity retention of 82.3% after 1000 cycles can be achieved at 10 A g<sup>-1</sup>. Through *in situ* synchrotron radiation-based X-ray diffraction, a sequential reversible proton and zinc-ion insertion/extraction process is verified, and the proton/zinc-ion dual-carrier co-insertion/extraction mechanism is highly responsible for the high capacity and rate of the aqueous ZIB system. Density functional theory analysis approve the low adsorption energy and preferential embedding of protons, which further optimizes the Zn<sup>2+</sup> adsorption and migration abilities in TBSNs by weakening the Coulombic ion-lattice interactions. As a result, an outward manifestation of a high pseudocapacitance proportion at high current rates is present and connected to the ultrafast ion migration capacity in the TBSNs.

## 2. Experimental Section

### 2.1. Fabrication of the thin Bi<sub>2</sub>Se<sub>3</sub> nanoplates

Bi(NO<sub>3</sub>)<sub>3</sub>·5H<sub>2</sub>O (99.0%), PVP 40000 (guaranteed reagent), selenium powder (99.0%), ethylenediamine (99.0%), L-ascorbic acid (99.7%), ZnSO<sub>4</sub>·7H<sub>2</sub>O (99.5%) and Bulk crystalline Bi<sub>2</sub>Se<sub>3</sub> (99.99%) were purchased from Sinopharm Chemical Reagent Co., Ltd. and used as received. The thin Bi<sub>2</sub>Se<sub>3</sub> nanoplates was prepared as follows. First, 0.5 g Bi(NO<sub>3</sub>)<sub>3</sub> and 0.6 g PVP 40000 were dissolved in 40 mL of ethanol and

mixed with a magnetic stirrer for 0.5 h to form a homogeneous solution. Then, 0.16 g of selenium powder was added, and 10 mL of ethylenediamine was added and mixed with a magnetic stirrer for another 10 min. After that, the uniformly mixed solution was transferred into a 100 mL Teflon-lined stainless-steel autoclave, and a solvothermal reaction was carried out at 150°C for 20 h. Subsequently, when the autoclave was cooled to room temperature, 0.5 g of L-ascorbic acid was added and stirred uniformly. The solution continued to react in the autoclave at 150°C for 5 h. The solid product was then collected by suction filtration and washed a few times with deionized water and ethanol. After annealing at 300°C under the protection of argon for 200 min, the thin Bi<sub>2</sub>Se<sub>3</sub> nanoplates was finally obtained. The bulk Bi<sub>2</sub>Se<sub>3</sub> powders were prepared by grinding the as-received sample in agate mortar for one hour.

### 2.2. Materials Characterization

The morphology, composition, and structure of the Bi<sub>2</sub>Se<sub>3</sub> nanoplates were studied by scanning electron microscopy (SEM, Carl Zeiss Gemini SEM 300), X-ray photoelectron spectroscopy (XPS, Kratos Analytical Axis UltraDLD) and transmission electron microscopy (TEM, JEM-2100). X-ray diffraction (XRD) patterns of the samples were obtained at BL14B1 using a MarCCD area detector. Atomic force microscopy (AFM, CSPM-5500) was used to assess the height of the Bi<sub>2</sub>Se<sub>3</sub> nanoplates. <sup>1</sup>H NMR were performed on ADVANCE NEO spectrometer with a 700MHz magnet, using 1.9 mm rotors operating at a spinning speed of 45 kHz.

### 2.3. Electrochemical Measurements

The electrochemical performance of the Bi<sub>2</sub>Se<sub>3</sub> nanoplates was tested via CR2025 coin-type cells from 0.2–1.7 V. The Bi<sub>2</sub>Se<sub>3</sub> cathode was prepared by mixing the Bi<sub>2</sub>Se<sub>3</sub> nanoplates, carbon black, and polyvinylidene fluoride (PVDF) in a mass ratio of 7:2:1 in 1-methyl-2-pyrrolidinone (NMP). Then, the slurry was coated on carbon paper and dried under vacuum at 80°C for 12 h. The mass loading of the active materials was approximately 1.0 mg cm<sup>-2</sup>. The full cells were assembled using the Bi<sub>2</sub>Se<sub>3</sub> nanoplates and Zn foil as the cathode and anode, a glass fibre membrane as the separator and 1M ZnSO<sub>4</sub> as the electrolyte. The bulk Bi<sub>2</sub>Se<sub>3</sub> electrode was fabricated from commercial Bi<sub>2</sub>Se<sub>3</sub> powders with the same approach. The galvanostatic charge-discharge test was carried out on a LANHE CT2001A battery testing system. The cyclic voltammetry test was performed on a CHI 760E (Chenhua Instrument Company, Shanghai, China) electrochemical workstation.

### 2.4. In situ Synchrotron Radiation-Based X-ray Diffraction Experiment

*In situ* XRD experiments were performed in the beamline BL14B1 (X-ray wavelength of 0.6887 Å) and BL02U2 (X-ray wavelength of 0.8857 Å) of the Shanghai Synchrotron Radiation Facility (SSRF). The beam size was confined by horizontal and vertical slits to be approximately 0.3 × 0.3 mm<sup>2</sup>. The two-dimensional XRD signal was acquired by a MarCCD detector with a typical time of approximately 4 min for one scan. Moreover, an *in situ* XRD study was carried out using a special coin cell. There were two observation holes with a radius of ~2 mm in the middle of both the cathode and anode side, guaranteeing that X-rays could penetrate through the active materials while cycling. The observation hole of the specially made *in situ* cell was sealed by polyimide tape. The electrochemical current density used for the *in situ* experiment was 0.08 A g<sup>-1</sup>.

### 2.5. Computational Methods

First-principles calculations based on density functional theory (DFT) were performed by the Vienna ab initio Simulation Package

(VASP) code. The Perdew-Burke-Ernzerhof (PBE) form within the generalized gradient approximation (GGA) and the projector augmented wave (PAW) pseudopotentials were used to describe the electron exchange-correlation potential and core electrons, respectively. In addition, the DFT-D3 method proposed by Grimme was also adopted to provide a better description of the long-range van der Waals interactions between the  $\text{Bi}_2\text{Se}_3$  layer and adatoms. The kinetic energy cutoff for the plane-wave basis was set to 400 eV. A vacuum layer of 20 Å along the z-axis was built to prevent interactions from periodic images. During structural optimization, all atoms were fully relaxed with a force convergence criterion of 0.01 eV/Å. Monkhorst-Pack k-point sampling ( $3 \times 3 \times 1$ ) was utilized for the Brillouin zone integration. The adsorption energy ( $\Delta E_{ads}$ ) of the Zn atom absorbed on the  $\text{Bi}_2\text{Se}_3$  layer with and without the pre-adsorption of H atoms was calculated by the following definition:  $\Delta E_{ads} = E_{sub-Zn} - E_{sub} - E_{Zn}$ , where  $E_{sub-Zn}$  and  $E_{sub}$  are the total energy of the  $\text{Bi}_2\text{Se}_3$  or  $\text{Bi}_2\text{Se}_3$ -H system with and without Zn atoms, respectively; and  $E_{Zn}$  is the total energy of Zn atoms.

### 3. Results and Discussion

The TBSNs were synthesized via a simple two-step solvothermal approach and compared with bulk  $\text{Bi}_2\text{Se}_3$  (Supplementary Fig. S1). Fig. 1a-b present the scanning electron microscopy (SEM) images of the as-

prepared TBSNs, showing a nanoplate morphology with a transverse size of approximately 500 nm. Energy-dispersive X-ray spectra (EDX) elemental mapping of the TBSNs reveals that the Bi elemental mapping image overlapped well with the Se image, showing the uniform distribution of Bi and Se. To further investigate the thickness of the TBSN, the synthesized materials are gently dispersed on silicon wafers and detected by SEM (Fig. 1c) and atomic force microscopy (AFM) (Fig. 1d). The results indicate a small diameter and uniform size. The average topographic height obtained by AFM analysis is  $\sim 5$  nm, corresponding to 4-6 quintuple layers (Fig. 1e). [30] The special multi-layer structure is considered to provide sufficient space for ion storage and effectively decrease the ion-diffusion distance. X-ray diffraction (XRD) pattern of the obtained TBSNs is shown in Fig. 1f. The TBSNs display a high degree of crystallization, and all the diffraction peaks can be indexed to layered orthorhombic  $\text{Bi}_2\text{Se}_3$  (JCPDS No. 33-0214). The crystal structure of  $\text{Bi}_2\text{Se}_3$  shown in the illustration of Fig. 1f consists of five covalently bonded atomic sheets that are ordered Se-Bi-Se-Bi-Se, thus forming a quintuple layer. To further investigate the structure of the TBSNs, transmission electron microscopy (TEM) and selected area electron diffraction (SAED) were conducted. Fig. 1g and Supplementary Fig. S2 show the whole view of the nanoplate structure. The size of the TBSNs ranges from 0.5-1  $\mu\text{m}$ , which is consistent with the SEM results. The unique thin nanoplate structure can effectively alleviate the large volume ex-

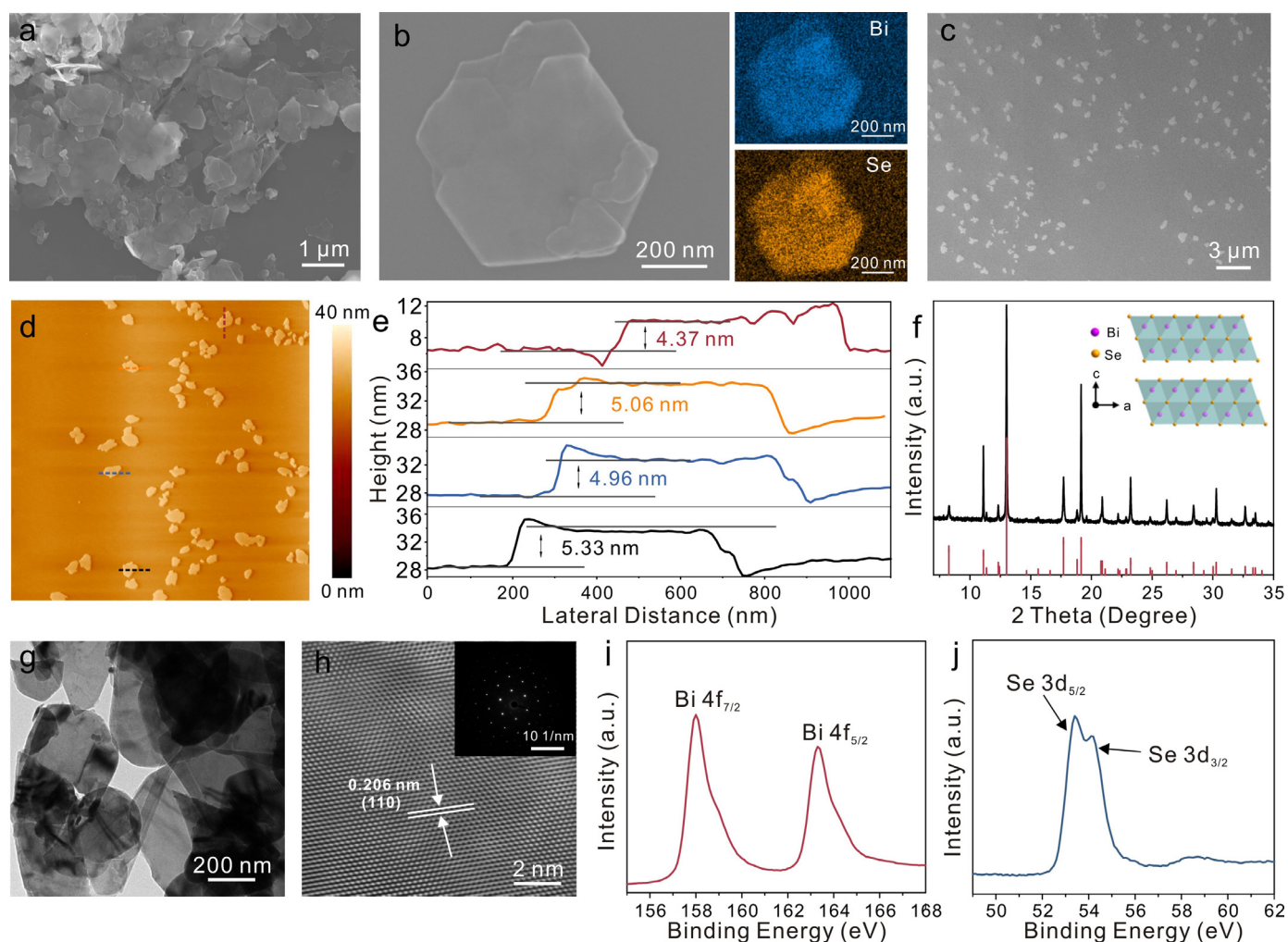


**Fig. 1.** (a-b) SEM images of the dense products and corresponding EDS analysis of Bi and Se. (c) SEM images of the TBSNs on the silicon substrate after dispersion. (d) AFM images of the TBSNs (left) and (e) corresponding AFM height profiles (right). (f) XRD pattern of the as-prepared TBSNs (inset is the crystallographic structure). (g) Low-resolution TEM images of the TBSNs. (h) High-resolution TEM image of the TBSNs, inset: the corresponding SAED pattern of the  $\text{Bi}_2\text{Se}_3$  nanoplates. (i) Bi 4f and (j) Se 3d fine spectra of the TBSNs after exposure to circumstance for more than 3 months.

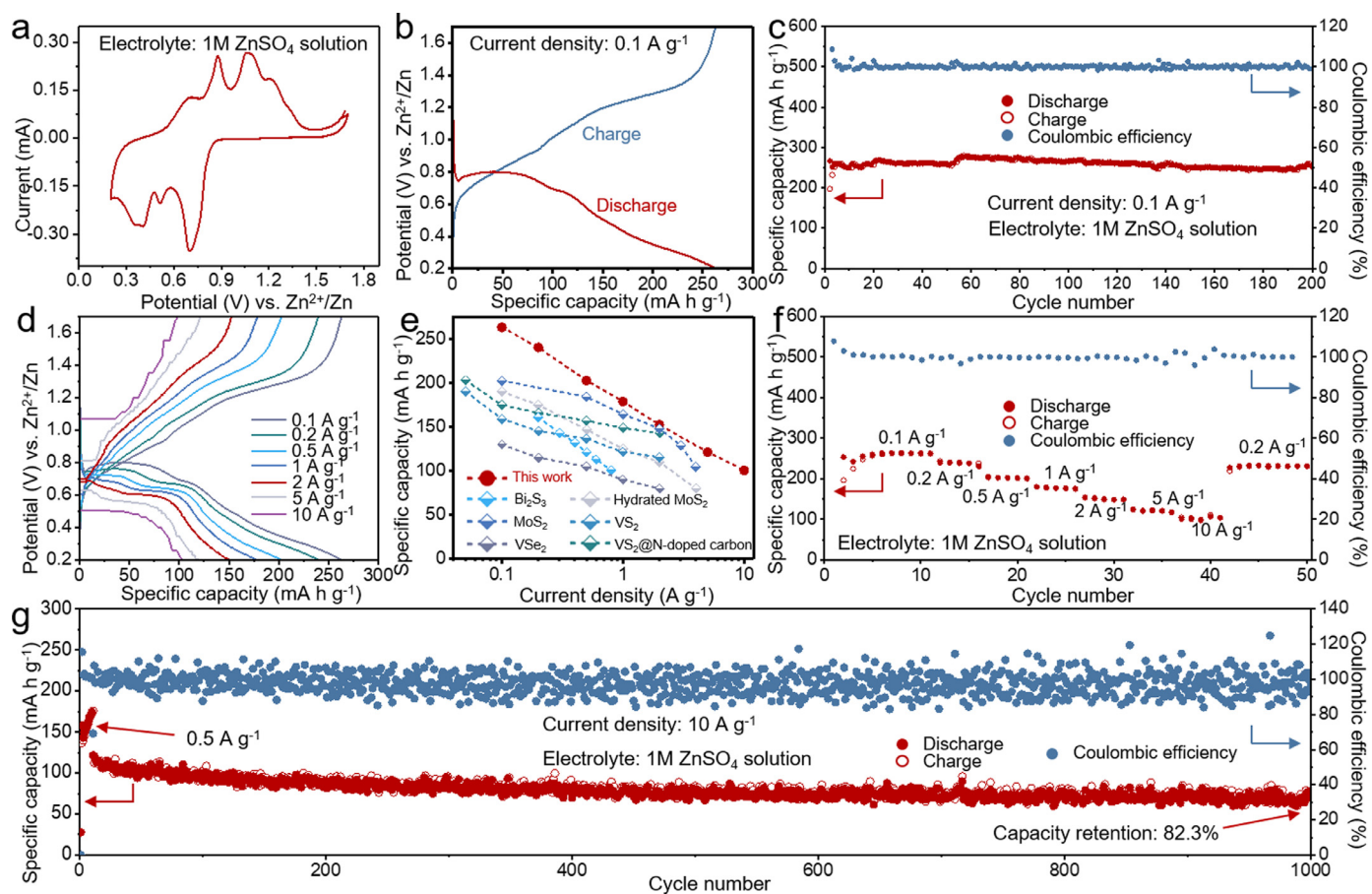


**Fig. 2.** Electrochemical performance of the TBSNs as a cathode material for ZIBs in 1M ZnSO<sub>4</sub> solution. (a) Cyclic voltammograms at a scan rate of 0.1 mV s<sup>-1</sup>. (b) Galvanostatic charge/discharge curves at 0.1 A g<sup>-1</sup>. (c) Cycling performance of the TBSN cathodes at 0.1 A g<sup>-1</sup>. (d) Charge-discharge profiles of the TBSN cathode at various current densities. (e) Rate performance comparison between the TBSN cathode and previously reported metal chalcogenide cathode materials for aqueous ZIBs, such as VSe<sub>2</sub>, VS<sub>2</sub>, Bi<sub>2</sub>S<sub>3</sub>, MoS<sub>2</sub>, hydrated MoS<sub>2</sub>, and VS<sub>2</sub>@N-doped carbon. (f) Rate capability of the TBSNs at various current densities, and (g) the cycling life of the TBSN cathode at 10 A g<sup>-1</sup>.

pansion, thereby achieving steady electrochemical performance without deforming the electrode microstructure after multiple cycles.[31] High resolution TEM (HRTEM) of the TBSNs shows a lattice spacing of 0.206 nm, which corresponds to the (110) crystal plane of Bi<sub>2</sub>Se<sub>3</sub> (Fig. 1h). Selective area electron diffraction (SAED) pattern confirms the high crystallinity of the synthesized TBSN. To explore the elemental composition, bonding and chemical stability of the TBSNs, X-ray photoelectron spectroscopy (XPS) was performed using TBSNs after exposure to circumstance for more than 3 months. The results clearly indicate the presence of Bi and Se in the TBSNs, where the binding energies are corrected by the presence of adventitious C 1s at 284.6 eV (Supplementary Fig. S3). The peaks of the 4f<sub>5/2</sub> and 4f<sub>7/2</sub> core levels of Bi clearly appear at 163.3 and 158 eV, respectively (Fig. 1i), and the 3d<sub>3/2</sub> and 3d<sub>5/2</sub> core levels of Se are located at 54.1 and 53.4 eV (Fig. 1j), which are in agreement with the pure Bi<sub>2</sub>Se<sub>3</sub> bulk (Supplementary Fig. S4). These results illustrate the high stability of the prepared Bi<sub>2</sub>Se<sub>3</sub> nanoplates.

The electrochemical performance of the TBSNs was evaluated by assembling a Zn/Bi<sub>2</sub>Se<sub>3</sub> cell utilizing TBSNs as the cathode, zinc foil as the anode, and 1M ZnSO<sub>4</sub> solution as the electrolyte. Fig. 2a displays the cyclic voltammetry (CV) curves of the TBSNs at 0.1 mV s<sup>-1</sup> in the voltage window of 0.2–1.7 V. Two pairs of redox peaks can be observed at approximately 0.7/1.0 V and 0.4/0.8 V, which can be ascribed to the occurrence of reversible ion insertion/extraction. Furthermore, the galvanostatic discharge/charge (GCD) curves at a current density of 0.1 A g<sup>-1</sup> show two plateaus in both the charge and discharge processes in Fig. 2b, which is in accordance with the CV curves. The cycling per-

formance of TBSNs was tested at a low current density of 0.1 A g<sup>-1</sup>. The cycling data in Fig. 2c shows a discharge capacity of 263.4 mA h g<sup>-1</sup> after 200 cycles with almost no capacity decay, and the Coulombic efficiency approaches 100% during cycling. In contrast, the Bi<sub>2</sub>Se<sub>3</sub> bulk electrode exhibits lower capacities and decay rapidly than the TBSNs (Supplementary Fig. S5). Therefore, it is considered that the superior rate performance of TBSNs was ascribed to the two-dimensional structure.[32] Fig. 2d and 2f show the charge-discharge curves and rate performance of the TBSNs. The discharge capacities are 263.2, 240.3, 202.7, 178.9, 152.4, 121.5 and 100.6 mA h g<sup>-1</sup> at 0.1, 0.2, 0.5, 1, 2, 5, 10 A g<sup>-1</sup>, respectively, far surpassing that of the Bi<sub>2</sub>Se<sub>3</sub> bulk electrode (Supplementary Fig. S6). In addition, when the current density returns to 0.2 A g<sup>-1</sup> after cycling for 40 cycles, the specific capacity recovers back to 231.2 mA h g<sup>-1</sup>, indicating the high reversibility of the reactions and fast charge storage kinetics. Such rate capability outperforms most previously reported metal chalcogenide cathodes (such as VSe<sub>2</sub>,[33] VS<sub>2</sub>,[19] Bi<sub>2</sub>S<sub>3</sub>,[25] MoS<sub>2</sub>,[20] hydrated MoS<sub>2</sub>,[34] and VS<sub>2</sub>@N-doped carbon [35]) and enables a superb power density of 4750 W kg<sup>-1</sup> at an energy density of 115.425 W h kg<sup>-1</sup> based on the active materials mass of cathode (Fig. 2e and S6). The long-term cycle performance was evaluated at high current of 10 A g<sup>-1</sup>. As shown in Fig. 2g, the TBSN cathode remains at 82.8 mA h g<sup>-1</sup> with 82.3% capacity retentions (compared with rate capacity at 10 A g<sup>-1</sup>) after 1000 cycles, thereby demonstrating the good cycling stability of the prepared Bi<sub>2</sub>Se<sub>3</sub> nanoplates. In contrast, bulk Bi<sub>2</sub>Se<sub>3</sub> can only maintain discharge capacities of 48.9 mA h g<sup>-1</sup> after 1000 cycles at 10 A g<sup>-1</sup> (Supplementary

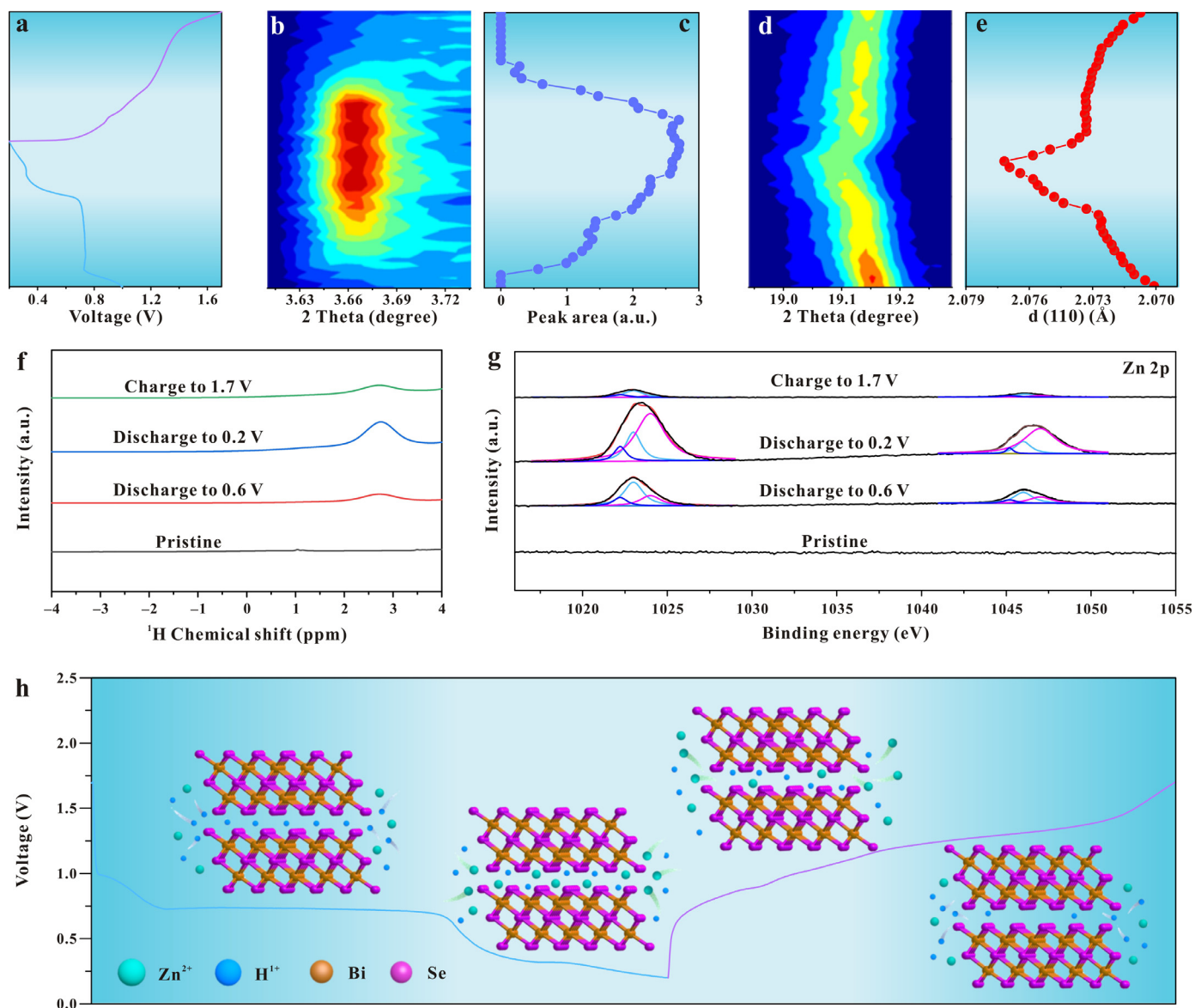


**Fig. 3.** Analysis of the ion storage mechanism for the TBSN cathode. (a) Galvanostatic charge-discharge curves between 0.2–1.7 V at  $0.08 \text{ A g}^{-1}$  ( $3\text{M ZnSO}_4$  solution) during the *in situ* observation. (b) *In situ* XRD patterns (X-ray wavelength of  $0.6887 \text{ \AA}$ ) of the (001) Bragg peak and (c) the corresponding peak area of the  $\text{Zn}_4\text{SO}_4(\text{OH})_6 \cdot 5\text{H}_2\text{O}$  byproduct during the second discharge-charge scan. (d) *In situ* XRD patterns of the (110) Bragg peak and (e) the related crystalline interplanar spacing changes in the TBSNs during the second discharge-charge scan as a function of the discharge and charge voltage. (f) Solid state  $^1\text{H}$  NMR at selected states and (g) XPS spectra of Zn 2p. (h) Schematic illustration showing the  $\text{Zn}^{2+}/\text{H}^+$  insertion/extraction in the TBSNs.

Fig. S8). The electrochemical performance of the TBSN is further investigated in high-concentration electrolyte ( $3\text{M ZnSO}_4$  solution). As expected, on the one hand, a much higher specific capacity of  $327 \text{ mA h g}^{-1}$  at  $0.2 \text{ A g}^{-1}$  and rate capacity of  $111 \text{ mA h g}^{-1}$  at  $20 \text{ A g}^{-1}$  (Supplementary Fig. S7) can be concurrently achieved due to the dense ions ( $\text{Zn}^{2+}$  and  $\text{H}^+$ ) surroundings; [36] on the other hand, the more strong acidic chemical environment caused by the enrichment of  $\text{H}^+$  will accelerate the corrosion of zinc foil and eventually lead to inferior cyclability [37]. Given the above, the feasibility of TBSN as a potential high-performance cathode for ZIBs can be concluded.

The galvanostatic charge and discharge processes between 0.2–1.7 V at a low current density of  $0.08 \text{ A g}^{-1}$  are shown in Fig. 3a. Simultaneously, *in situ* XRD is conducted to analyse the phase evolution of the TBSN cathode to further understand the energy storage mechanism (Supplementary Fig. S8). Notably, the new diffraction peak observed at  $3.66^\circ$  during the discharge process can be indexed to  $\text{Zn}_4\text{SO}_4(\text{OH})_6 \cdot 5\text{H}_2\text{O}$  (Fig. 3b). The formation of  $\text{Zn}_4\text{SO}_4(\text{OH})_6 \cdot 5\text{H}_2\text{O}$

was also proved by the SEM images. Compared to the initial TBSN electrode, obvious flakes are observed on the surface of the TBSN electrode discharged to  $0.7 \text{ V}$  (Supplementary Fig. S9). Besides, SEM-EDS results verify that the flake is  $\text{Zn}_4\text{SO}_4(\text{OH})_6 \cdot 5\text{H}_2\text{O}$  due to the fact that there are Zn, O, and S in the flakes (Supplementary Fig. S10). The formation of the alkaline  $\text{Zn}_4\text{SO}_4(\text{OH})_6 \cdot 5\text{H}_2\text{O}$  byproduct is ascribed to the massive consumption of protons by the cathode in the weakly acidic  $\text{ZnSO}_4$  electrolyte. Due to the small radius of protons, the intercalation process of protons into the lattice of the TBSN cathode is kinetically easier than  $\text{Zn}^{2+}$  during the initial discharge process ( $\sim 0.7 \text{ V}$ ). As a result, more protons will be supplemented by the decomposition of  $\text{H}_2\text{O}$  in the electrolyte to generate  $\text{H}^+$  and  $\text{OH}^-$ . Additionally, the obtained  $\text{OH}^-$  can coordinate with the  $\text{ZnSO}_4$  electrolyte to spontaneously form  $\text{Zn}_4\text{SO}_4(\text{OH})_6 \cdot 5\text{H}_2\text{O}$ . Until an energy balance is reached between the ionization efficiency of  $\text{H}_2\text{O}$  and the adsorption energy of  $\text{H}^+$  in the TBSN cathode, the  $\text{H}^+$  insertion process may be limited, which is reflected by the constant (001) peak area of the

Zn<sub>4</sub>SO<sub>4</sub>(OH)<sub>6</sub>•5H<sub>2</sub>O byproduct (emphasized by the light blue region in Fig. 3c). Zn<sub>4</sub>SO<sub>4</sub>(OH)<sub>6</sub>•5H<sub>2</sub>O gradually disappears after charging from 0.9 to 1.3 V. These phenomena indicate the reversible generation/decomposition of Zn<sub>4</sub>SO<sub>4</sub>(OH)<sub>6</sub>•5H<sub>2</sub>O on the cathode during the discharge/charge process. To clarify the structural evolution of the TBSNs during the charge and discharge processes, the characteristic peak located at 19.1° (reflection of the (001) plane of Bi<sub>2</sub>Se<sub>3</sub>) is enlarged, as shown in Fig. 3d. The diffraction peak shifts to a small angle during the discharge process and recovers to the original state during the charge process, revealing a typically reversible insertion/extraction reaction of the TBSN cathode, consistent with SEM images (Supplementary Fig. S9). Fig. 3e displays the evolution of the d (110) value of Bi<sub>2</sub>Se<sub>3</sub> according to the *in situ* XRD results. The increase of the d (110) plane value during discharge can be divided into two parts. The increased amplitude of the d (110) value is relatively small at the initial discharging stage, corresponding to the high production of the Zn<sub>4</sub>SO<sub>4</sub>(OH)<sub>6</sub>•5H<sub>2</sub>O byproduct (Fig. 3c) and indicating exclusive H<sup>+</sup> insertion. When the (001) peak area of the Zn<sub>4</sub>SO<sub>4</sub>(OH)<sub>6</sub>•5H<sub>2</sub>O byproduct becomes stable, the production of Zn<sub>4</sub>SO<sub>4</sub>(OH)<sub>6</sub>•5H<sub>2</sub>O ends, signifying that the proton insertion process is terminated (the light blue region in Fig. 3c). At this time, the increase in the d (110) plane value suddenly accelerates, which means Zn<sup>2+</sup> insertion is occurring in the TBSN cathode due to the larger radius of Zn<sup>2+</sup> than H<sup>+</sup> (the light blue region in Fig. 3e). These results indicate that the intercalation of Zn<sup>2+</sup> and H<sup>+</sup> is carried out sequentially rather than simultaneously. During the charging process, the d (110) of Bi<sub>2</sub>Se<sub>3</sub> and (001) peak area of Zn<sub>4</sub>SO<sub>4</sub>(OH)<sub>6</sub>•5H<sub>2</sub>O recover to the initial state after strictly following the sequential steps. The above results clearly confirm the highly reversible dual-carrier storage in the aqueous Zn/Bi<sub>2</sub>Se<sub>3</sub> system, which undergoes a different sequence of H<sup>±</sup> and Zn<sup>2±</sup> insertion/extraction and maintains consistency in the stable cycles with electrolytes of various concentrations (Supplementary Fig. S11).

To further confirm the sequential insertion/extraction of H<sup>+</sup> and Zn<sup>2+</sup> in the TBSNs during the charge/discharge process, the TBSN-based positive electrodes at the selected charge/discharge states were investigated by the solid state 1H NMR and XPS spectra respectively (Fig. 3f and 3g). As shown in Fig. 3f, compared with the initial state of the TBSN electrodes, there appears a new peak at 2.7 ppm when the battery discharge to 0.6 V, which would be ascribed to the H<sup>+</sup> that inserted in the TBSN. However, the intensity of this peak is slightly enhanced at discharge stage from 0.6 V to 0.2 V, which probably because a small amount of H<sup>+</sup> insert into TBSN. Subsequently, at the charge stage from 0.2 V to 1.7 V, the intensity of this peak decreased, indicating that H<sup>+</sup> was reversibly extracted from the TBSN. Meanwhile, XPS spectra were employed to confirm the insertion/extraction of Zn<sup>2+</sup>, as shown in Fig. 3g. In the Zn 2p spectra of TBSN electrodes, three pairs of Zn<sup>2+</sup> peaks located at 1022.2/1045.2, 1023/1046, 1024/1047 eV are assigned to the inserted Zn<sup>2+</sup> in Zn(OH)<sub>2</sub>, ZnSO<sub>4</sub> from Zn<sub>4</sub>SO<sub>4</sub>(OH)<sub>6</sub>•5H<sub>2</sub>O, and Zn<sup>2+</sup> in TBSN, respectively. At the discharge stage from 0.6 to 0.2 V, it is noted that there is a distinct increase in the intensity of peaks belonging to the inserted Zn<sup>2+</sup> in the TBSN while the peak area of the Zn<sup>2+</sup> from Zn<sub>4</sub>SO<sub>4</sub>(OH)<sub>6</sub>•5H<sub>2</sub>O byproduct remains unchanged. It reveals that a large quantity of Zn<sup>2+</sup> insert to TBSN during this discharge process. The peak of the Zn<sup>2+</sup> in the TBSN is obviously decreased and nearly recovers to the initial state at the charge stage from 0.2 V to 1.7 V. It suggests that the Zn<sup>2+</sup> in the TBSN can reversibly extracted from the TBSN during cycling. Furthermore, the peaks of the Zn<sup>2+</sup> in Zn(OH)<sub>2</sub> and Zn<sup>2+</sup> from Zn<sub>4</sub>SO<sub>4</sub>(OH)<sub>6</sub>•4H<sub>2</sub>O also exhibit a similar trend, revealing the reversible conversion of Zn<sub>4</sub>SO<sub>4</sub>(OH)<sub>6</sub>•4H<sub>2</sub>O during cycling. Therefore, based on the above discussion, it is verified that H<sup>+</sup> and Zn<sup>2+</sup> can successively insert into and extract from TBSN during cycling. The illustration of the entire reaction mechanism of the TBSN cathode is depicted vividly in Fig. 3h. The sequential dual-insertion mechanism may benefit charge transfer, thus resulting in a high theoretical capacity and good electrochemical performance.

The ion storage and kinetics properties of the TBSN cathode were carried out by consecutive CV measurements at various scan rates from

0.1 to 0.6 mV s<sup>-1</sup> (Fig. 4a). The redox peaks of Peak 1 and 3 correspond to the (de)intercalation process of Zn<sup>2+</sup>, while Peak 2 and 4 are related to the (de)intercalation process of protons. In general, the peak current (*i*) response in the CV curves obeys the power law according to the equation described as follows:

$$i = av^b \quad (1)$$

where *i* is the current, *v* is the scan rate, and *a* and *b* are adjustable parameters. [38] The *b*-value is determined from the slope of the log (*i*) versus log (*v*) plot. Diffusion-controlled behaviour dominates when the *b*-value approaches 0.5, and on the other hand, surface-driven behaviour, *viz.*, the capacitive process, dominates as the *b*-value increases to nearly 1.0. [39] It was calculated that the *b*-values of Peaks 1-4 are 0.7, 0.8, 0.78, and 0.99, respectively (Fig. 4b), demonstrating the presence of a synergistic charge storage process that includes both diffusion-controlled and capacitive behaviours coexisting in the TBSNs. In addition, the CV curves show a similar shape at various scan rates from 0.1 to 0.6 mV s<sup>-1</sup> (Fig. 4a), suggesting the small polarization voltage and fast kinetics of the TBSN cathode. To further specify the capacitive contribution at a certain scan rate, the following equations:

$$i = k_1v + k_2v^{1/2} \quad (2)$$

and

$$i/v^{1/2} = k_1v^{1/2} + k_2 \quad (3)$$

are employed to evaluate the capacity ratio between the capacitive (*k*<sub>1</sub>*v*) and diffusion-controlled (*k*<sub>2</sub>*v*<sup>1/2</sup>) behaviour at a particular voltage during cycling. [40] With increasing scan rates from 0.1 to 0.5 mV s<sup>-1</sup>, the capacitive contribution ratios increase from 63% to a dominant position of 85% at 0.5 mV s<sup>-1</sup> (Fig. 4c). Therefore, it is concluded that the high rate performance of the TBSNs is attributed to the prominent capacitive-controlled kinetics process. The abovementioned analysis explains the origin of the excellent capability of the TBSN electrode at a high rate.

To further interpret the experimental results, we performed a theoretical investigation of the superior ion storage and diffusion properties of the TBSNs by performing a series of density functional theory (DFT) calculations. According to the proposed kinetic process, the adsorption energies of the Zn-ions and protons on the original Bi<sub>2</sub>Se<sub>3</sub> surface were calculated to illustrate the selective adsorption during the cycle. All atoms were fully relaxed with a force convergence criterion of 0.01 eV/Å during the structural optimization. Consistent with the XRD and CV measurements, Bi<sub>2</sub>Se<sub>3</sub> shows a lower adsorption energy for protons with values of -1.01 eV at the Top, -0.59 eV at the Hollow and -0.12 eV at the Valley (Supplementary Fig. S12) than for Zn-ions with values of 0.60 eV at the Top, -0.05 eV at the Hollow, 0.30 eV at the Valley (Supplementary Fig. S13), suggesting the preference for the proton embedding process. The binding energy of the Bi<sub>2</sub>Se<sub>3</sub> surface for proton, with varies proportionally of the protons occupying number, is also calculated to further evaluate the occupation trend. The calculated binding energy for H<sub>*x*</sub>Bi<sub>2</sub>Se<sub>3</sub> is -0.91 eV for H<sub>0.33</sub>Bi<sub>2</sub>Se<sub>3</sub>, -0.86 eV for H<sub>0.5</sub>Bi<sub>2</sub>Se<sub>3</sub>, -0.89 eV for HBi<sub>2</sub>Se<sub>3</sub>, and -0.94 eV for H<sub>2</sub>Bi<sub>2</sub>Se<sub>3</sub>. It can be clearly seen that with the increase in the proportion of protons on the surface, Bi<sub>2</sub>Se<sub>3</sub> exhibits a stable binding energy, which is conducive to the capture and storage of protons and leads to complete proton occupation on the surface after the termination of proton intercalation (Supplementary Fig. S14). Subsequently, after being occupied completely by protons, the adsorption capability of Zn-ions is greatly improved (Δ*E* = -1.11 eV, lower adsorption energy) compared with the original surface (Supplementary Fig. S15). Therefore, the second ion insertion, *i.e.*, the Zn<sup>2+</sup> insertion progress, also shows excellent capacity. Furthermore, considering the results of the *in situ* XRD measurements and the above discussion, we calculated the energy barriers of the migration of Zn<sup>2+</sup> on the original Bi<sub>2</sub>Se<sub>3</sub> surface and the Bi<sub>2</sub>Se<sub>3</sub> surface completely occupied by H<sup>+</sup> to match the actual charge/discharge process and the analysis results of the binding energy of H<sub>*x*</sub>Bi<sub>2</sub>Se<sub>3</sub>. For the original Bi<sub>2</sub>Se<sub>3</sub>, the inserted Zn-ions possess three possible diffusion paths: Hollow-Hollow (H-H, Path

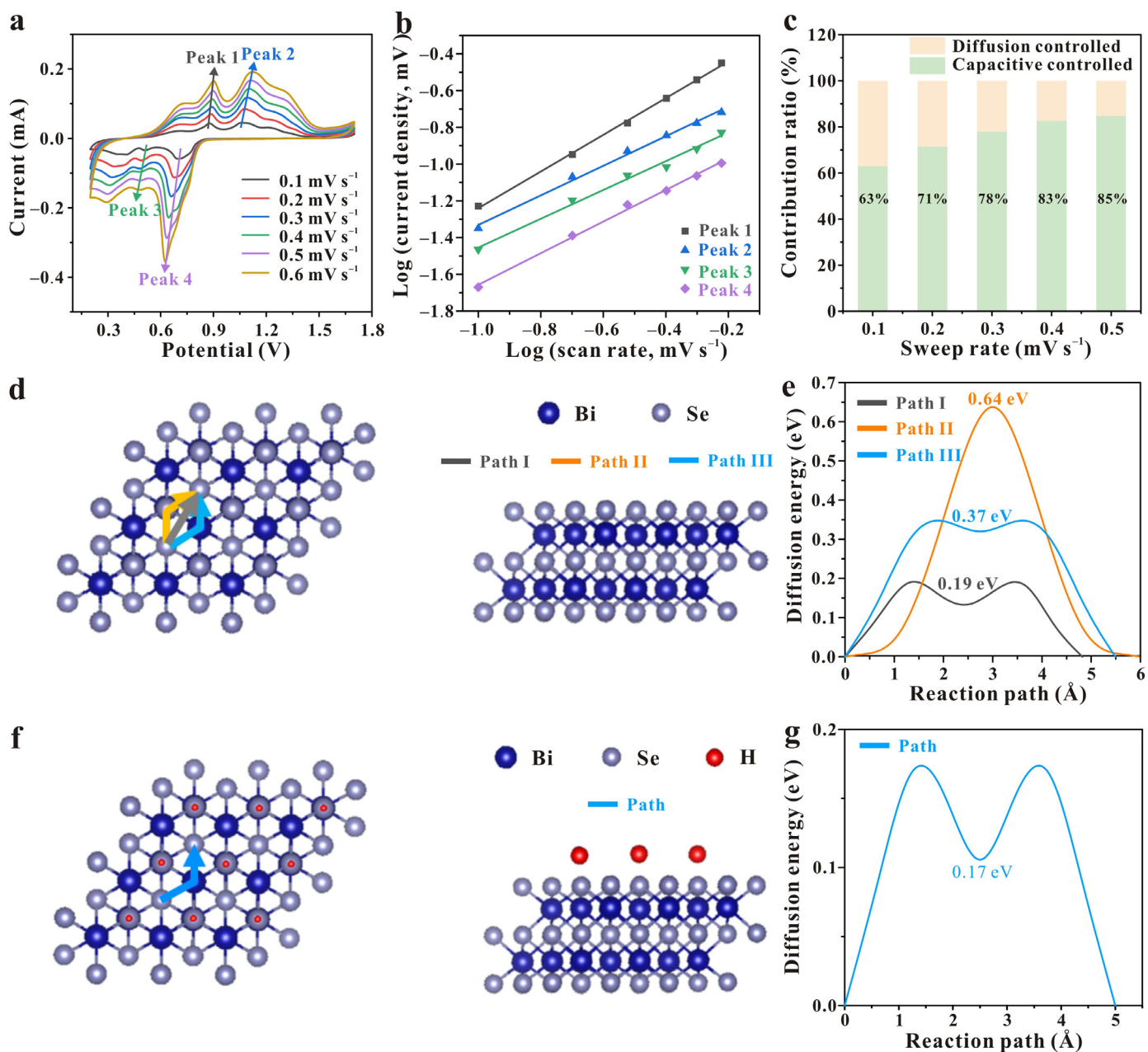


**Fig. 4.** Kinetics analysis and mechanism of the ion storage process of the TBSNs. (a) CV curves of the TBSNs tested at different scan rates from 0.1 to 0.6  $\text{mV s}^{-1}$ . (b) Log ( $i$ ) versus log ( $v$ ) curves of the cathodic and anodic peaks, and (c) contribution ratios of the normalized capacitive (light orange) and diffusion-controlled (light green) peaks from 0.1 to 0.5  $\text{mV s}^{-1}$ . (d) Top view and side view of the original  $\text{Bi}_2\text{Se}_3$  surface and the marked path (Path I, Path II and Path III) of the Zn-ion migration. (e) Migrated energy barriers on the original  $\text{Bi}_2\text{Se}_3$  surface that correspond to Path I, Path II and Path III. (f) Top and side view of the  $\text{Bi}_2\text{Se}_3$  surface completely occupied by protons and the marked path of the Zn-ion migration. (g) Migrated energy barriers on the  $\text{Bi}_2\text{Se}_3$  surface completely occupied by protons.

I), Hollow-Top-Hollow (H-T-H, Path II) and Hollow-Valley-Hollow (H-V-H, Path III). The calculated energy barriers of  $\text{Bi}_2\text{Se}_3$  corresponding to the different paths are shown in Fig. 4d-e. Path I is considered to be the most likely diffusion mode as it is the migration path with the lowest diffusion barrier (0.19 eV). For the stable  $\text{Bi}_2\text{Se}_3$  surface completely occupied by protons, Zn-ions show isotropic migration and have an appropriate diffusion barrier as low as 0.17 eV (Fig. 4f and g), which is lower than that of any possible migration path on the original pure  $\text{Bi}_2\text{Se}_3$ . This result is consistent with the observed ion insertion process in the batch experiments, in which the protons inserted first promote the diffusion of the Zn-ions that are subsequently embedded. This process is beneficial for achieving excellent capacity and fast kinetics at high rates and further illuminates the excellent performance and high reversible capacity of TBSN cathodes in aqueous ZIBs.

#### 4. Conclusion

In summary, thin  $\text{Bi}_2\text{Se}_3$  nanoplates are synthesized by a simple hydrothermal method and introduced as aqueous ZIB cathodes for the first time. These nanoplates deliver a high specific capacity of 263.2  $\text{mA h g}^{-1}$  at 0.1  $\text{A g}^{-1}$ , ideal rate performance (100.6  $\text{mA h g}^{-1}$  at 10  $\text{A g}^{-1}$ ), and decent cycling stability (82.3% retention after 1000 cycles). A sequential proton and Zn-ion insertion/extraction process is captured by *in situ* synchrotron radiation-based X-ray diffraction, demonstrating a reversible dual-carrier storage mechanism. Furthermore, density functional theory analysis shows that the intercalation of protons *via* low adsorption energy occurs much more easily, which further optimizes the  $\text{Zn}^{2+}$  adsorption and migration abilities in the TBSNs by weakening the Coulombic ion-lattice interactions and leads to an outstanding rate

capability. As a result, the outward manifestation of a high pseudocapacitance proportion at high current rates is connected to the ultrafast ion migration capacity in the TBSNs. This new type of Bi<sub>2</sub>Se<sub>3</sub> cathode provides a promising choice for the development of high-performance aqueous ZIBs.

#### Declaration of competing interest

The authors declare that they have no known competing financial interests or personal relationships that could have appeared to influence the work reported in this paper.

#### Acknowledgments

This work was financially supported by the National Natural Science Foundation of China (No. 12005286, 11875315, U2032204, U1932201, U1732121), National Key Research and Development Programme of China (No. 2017YFA0403400, 2016YFA0401002), the Shanghai Sailing Programme (No. 19YF1452700), the CAS Pioneer “Hundred Talents Programme” (type C), the Science Challenge Project (No. TZ2018001), the Major Projects of Science and Technology Commission of Shanghai (No. 17JC1400800) and Natural Science Foundation of Shanghai (No. 20ZR1464200). The authors thank the Shanghai Synchrotron Radiation Facility (SSRF) BL08U, BL14B1, BL17B1, BL02U2 and BL15U1 staff.

#### Supplementary materials

Supplementary material associated with this article can be found, in the online version, at doi:10.1016/j.ensm.2021.07.015.

#### References

- [1] J.J. Liu, Y. Yang, P.B. Lyu, P. Nachtigall, Y.X. Xu, *Adv. Mater.* 30 (2018) 1800838.
- [2] B. Dunn, H. Kamath, J.M. Tarascon, *Science* 334 (2011) 928–935.
- [3] X. Hu, J. Sun, Z. Li, Q. Zhao, C. Chen, J. Chen, *Angew. Chem. Int. Ed.* 55 (2016) 6482–6486.
- [4] Y. Zhang, S. Liu, Y. Ji, J. Ma, H. Yu, *Adv. Mater.* 30 (2018) 1706310.
- [5] P. Xiong, F. Zhang, X. Zhang, S. Wang, H. Liu, B. Sun, J. Zhang, Y. Sun, R. Ma, Y. Bando, C. Zhou, Z. Liu, T. Sasaki, G. Wang, *Nat. Commun.* 11 (2020) 3297.
- [6] M.C. Lin, M. Gong, B. Lu, Y. Wu, D.Y. Wang, M. Guan, M. Angell, C. Chen, J. Yang, B.J. Hwang, H. Dai, *Nature* 520 (2015) 325–328.
- [7] Y. Yamada, K. Usui, K. Sodeyama, S. Ko, Y. Tateyama, A. Yamada, *Nat. Energy.* 1 (2016) 16129.
- [8] F. Wan, L. Zhang, X. Dai, X. Wang, Z. Niu, J. Chen, *Nat. Commun.* 9 (2018) 1656.
- [9] B. Häupler, C. Rössel, A.M. Schwenke, J. Winsberg, D. Schmidt, A. Wild, U.S. Schubert, *NPG Asia Mater* 8 (2016) 283–283.
- [10] X. Li, M. Li, Q. Yang, D. Wang, L. Ma, G. Liang, Z. Huang, B. Dong, Q. Huang, C. Zhi, *Adv. Energy Mater.* 10 (2020) 2001394.
- [11] C. Xu, B. Li, H. Du, F. Kang, *Angew. Chem. Int. Ed.* 51 (2012) 933–935.
- [12] M. Yan, P. He, Y. Chen, S. Wang, Q. Wei, K. Zhao, X. Xu, Q. An, Y. Shuang, Y. Shao, K.T. Mueller, L. Mai, J. Liu, J. Yang, *Adv. Mater.* 30 (2018) 1703725.
- [13] P. Canepa, G. Sai Gautam, D.C. Hannah, R. Malik, M. Liu, K.G. Gallagher, K.A. Persson, G. Ceder, *Chem Rev* 117 (2017) 4287–4341.
- [14] N. Zhang, F. Cheng, J. Liu, L. Wang, X. Long, X. Liu, F. Li, J. Chen, *Nat Commun* 8 (2017) 405.
- [15] L. Zhang, L. Chen, X. Zhou, Z. Liu, *Adv. Energy Mater.* 5 (2015) 1400930.
- [16] H. Pan, Y. Shao, P. Yan, Y. Cheng, K.S. Han, Z. Nie, C. Wang, J. Yang, X. Li, K.T. Mueller, P. Bhattacharya, J. Liu, *Nat. Energy.* 1 (2016) 16039.
- [17] H. Wang, J. Liu, H. Wang, X. Cai, X. Ye, L. Zhang, Z. Chen, Z.X. Shen, *J. Mater. Chem. A.* 8 (2020) 14900–14907.
- [18] T. Wang, D. Legut, Y. Fan, J. Qin, X. Li, Q. Zhang, *Nano Lett* 20 (2020) 6199–6205.
- [19] P. He, M.Y. Yan, G.B. Zhang, R.M. Sun, L.N. Chen, Q.Y. An, L.Q. Mai, *Adv. Energy Mater.* 7 (2017) 1601920.
- [20] H. Li, Q. Yang, F. Mo, G. Liang, Z. Liu, Z. Tang, L. Ma, J. Liu, Z. Shi, C. Zhi, *Energy Storage Mater* 19 (2019) 94–101.
- [21] W.W. Xu, C.L. Sun, K.N. Zhao, X. Cheng, S. Rawal, Y. Xu, Y. Wang, *Energy Storage Mater* 16 (2019) 527–534.
- [22] H. Liang, Z. Cao, F. Ming, W. Zhang, D.H. Anjum, Y. Cui, L. Cavallo, H.N. Alshareef, *Nano Lett* 19 (2019) 3199–3206.
- [23] J.P. Liu, P.T. Xu, J.M. Liang, H.B. Liu, W.C. Peng, Y. Li, F.B. Zhang, X.B. Fan, *Chem. Eng. J.* 389 (2020) 124405.
- [24] J.H. Huang, Z. Wang, M.Y. Hou, X.L. Dong, Y. Liu, Y.G. Wang, Y.Y. Xia, *Nat. Commun.* 9 (2018) 2906.
- [25] T. Xiong, Y.M. Wang, B.S. Yin, W. Shi, W.S.V. Lee, J.M. Xue, *Nano-Micro Lett* 12 (2019) 9.
- [26] H.J. Zhang, C.X. Liu, X.L. Qi, X. Dai, Z. Fang, S.C. Zhang, *Nat. Phys.* 5 (2009) 438–442.
- [27] A. Zhuang, J.J. Li, Y.C. Wang, X. Wen, Y. Lin, B. Xiang, X. Wang, J. Zeng, *Angew. Chem. Int. Ed. Engl.* 53 (2014) 6425–6429.
- [28] G. Han, Z.G. Chen, D.L. Ye, L. Yang, L.Z. Wang, J. Drennan, J. Zou, *J. Mater. Chem. A.* 2 (2014) 7109–7116.
- [29] L. Xie, Z. Yang, J. Sun, H. Zhou, X. Chi, H. Chen, A.X. Li, Y. Yao, S. Chen, *Nano-Micro. Lett.* 10 (2018) 50.
- [30] D.S. Kong, W.H. Dang, J.J. Cha, H. Li, S. Meister, H.L. Peng, Z.F. Liu, Y. Cui, *Nano Lett* 10 (2010) 2245–2250.
- [31] L. Ji, Z. Lin, M. Alcoutlabi, X. Zhang, *Energy Environ. Sci.* 4 (2011) 2682–2699.
- [32] T. Wei, Y. Liu, G. Yang, C. Wang, *Energy Storage Mater* 30 (2020) 130–137.
- [33] Z.Y. Wu, C.J. Lu, Y.N. Wang, L. Zhang, L. Jiang, W.C. Tian, C.L. Cai, Q. Gu, Z.M. Sun, L.F. Hu, *Small* 16 (2020) 2000698.
- [34] H. Liu, J. Wang, W. Hua, Z. You, Z. Hou, J. Yang, C. Wei, Kang F, *Energy Storage Mater* 35 (2021) 731–738.
- [35] J. Liu, W. Peng, Y. Li, F. Zhang, X. Fan, *J. Mater. Chem. C.* 9 (2021) 6308–6315.
- [36] A.S. Poyraz, J. Laughlin, Z. Zec, *Electrochimica Acta* 305 (2019) 423–432.
- [37] V. Verma, R.M. Chan, L. Jia Yang, S. Kumar, S. Sattayaporn, R. Chua, Y. Cai, P. Kidkhunthod, W. Manalastas, M. Srinivasan, *Chem. Mater.* 33 (2021) 1330–1340.
- [38] T. Brezesinski, J. Wang, S.H. Tolbert, B. Dunn, *Nature Mater* 9 (2010) 146–151.
- [39] J. Huang, X. Lin, H. Tan, B. Zhang, *Adv. Energy Mater.* 8 (2018) 1703496.
- [40] Q. Yang, F. Mo, Z. Liu, L. Ma, X. Li, D. Fang, S. Chen, S. Zhang, C. Zhi, *Adv Mater* 31 (2019) 1901521.